Moving-Source and Caloric-Curve Analyses of Reactions Induced by 1.8-4.8 GeV ^{3}He Beams on ^{nat}Ag and ^{197}Au Nuclei*

D.S. Bracken†, K. Kwiatkowski†, E. Renshaw Foxford‡, K.B. Morley†, V.E. Viola and N.R. Yoder

Indiana University Chemistry Department and IUCF, Bloomington, IN 47405

J. Brzychczyk

Institute of Physics, Jagellonian University, 30-059 Krakow, Poland

E.C. Pollacco, R. Legrain§, and C. Volant

DAPNIA/SPhN, CEA/Saclay, F-91191 Gif-sur-Yvette Cedex, France

R.G. Korteling

Department of Chemistry, Simon Fraser University, Burnaby V5A 1S6 Canada

H. Breuer

Department of Physics, University of Maryland, College Park, MD 20742

(October 28, 2003)

Abstract

*Research supported by the U.S. Department of Energy, the National Science Foundation, NSERC of Canada and CEA Saclay.

†Present address: Los Alamos National Laboratory, Los Alamos, NM 87545

†Present address: Los Alamos National Laboratory, Los Alamos, NM 87545

‡Present address: Microsoft Corp., Redmond, WA

§Deceased

Multifragment breakup of ^{nat}Ag and ^{197}Au nuclei bombarded by 1.8 - 4.8 GeV ^{3}He ions has been studied with the ISiS 4π detector array. To investigate the properties of the emitting source as a function of excitation energy, a two-component moving-source analysis has been performed on the IMF spectra, gating on excitation energy. The results provide evidence for nuclear expansion/dilution to a value of $\rho/\rho_0 \lesssim 1/3$ prior to breakup. For the most violent events, relatively low source velocities of v/c $\sim$ 0.01 and slope temperatures of T $\sim$ 15 MeV are obtained for the dominant thermal-like source. The dependence of isotope ratios on deposition energy and ejectile kinetic energy is examined for H and He isotopes, and the caloric curves for the 4.8 GeV data are presented.

25.70.Pq,25.55.e

I. INTRODUCTION

In light-ion-induced reactions at bombarding energies above a few GeV, central collisions produce highly excited residues that emit multiple intermediate-mass-fragments (IMF: $3 \leq Z \lesssim 15$) [1–3]. Multifragmentation is of interest because it appears to be associated with large excitation energies per residue nucleon E^*/A, approaching or exceeding the total nuclear binding energy/nucleon of the residue. For light-ion-induced reactions there is only a single heavy residue, and compression and angular momentum effects are predicted to be small [4]. Thus, by studying the decay of these systems, one hopes to gain a more complete understanding of the thermal properties of finite nuclei under extreme conditions of heat content.

Many of the early studies of IMF emission in light-ion-induced reactions employed radiochemical and emulsion techniques [5–7]. These studies, reviewed in [8–10], show a strong increase in IMF emission probability up to a bombarding energy of about 5 GeV, after which the cross sections become largely independent of projectile energy (limiting fragmentation) up to 50 GeV. The first exclusive measurements using electronic detection techniques were conducted by Warwick *et al.* [11], which indicated the existence of multiple IMF production in an event. Subsequent inclusive studies of the p + Kr, Xe [12] and ^{3}He + ^{nat}Ag [13] spectra suggested that a mechanism change occurs when the light-ion bombarding energy exceeds about 2 GeV. As a follow-up to the studies of Ref. [13], a limited coincidence measurement of the 3.6 GeV ^{3}He + ^{nat}Ag reaction was performed that emphasized detection of very low energy fragments [14]. This work provided evidence for significant multiplicities of IMFs in light-ion-induced reactions and further demonstrated that the most violent events produced a high yield of sub-Coulomb-energy ejectiles, suggestive of nuclear expansion/dilution prior to breakup of the hot residue [14,15].

The scenario for light-ion-induced multifragmentation that has emerged is the following. For central collisions the initial projectile-target interaction produces a shower of fast hadrons and coalescence light charged particles (LCP: $Z \leq 2$), leaving a highly excited residue in

a state of depleted density [4,16]. Within a time frame $\tau \lesssim 50$ fm/c, the system evolves toward an equilibrium-like final state, cooling by emitting preequilibrium LCPs and IMFs [17]. Finally the hot residue disintegrates statistically [18] into multiple neutrons, LCP's and IMF's on a time scale of order $\tau \sim$ 20-50 fm/c [19,20].

Recently, Natowitz *et al.* have addressed the important question of the breakup temperature and density of hot nuclei as a function of excitation energy and residue mass, of central concern in discussions of limiting temperatures and the nuclear equation of state [21]. In this paper, we deal with this question, as well as the properties of the hot residues formed in the collision stage. We employ a two-component, moving-source analysis to examine the IMF kinetic energy spectra as a function of collision violence. In addition, light-charged-particle isotope yields (LCP = H and He) are examined. These are then interpreted in the context of the mechanism for light-ion-induced multifragmentation and implications for caloric curve analyses [17,22,23].

II. EXPERIMENTAL MEASUREMENTS AND DATA ANALYSIS

Measurements were performed with the Indiana Silicon Sphere (ISiS) detector array at the Laboratoire National Saturne with beams of 1.8, 3.6 and 4.8 GeV ^{3}He ions incident on targets of ^{nat}Ag and ^{197}Au [24,25]. No data were taken at 3.6 GeV with the gold target. Target thicknesses were 1.1 and 1.5 mg/cm^2, respectively. Beam intensities were 5 - 10 $\times$ 10^7 particles/spill, with a spill time of 500 ms.

The ISiS array [26] was used to obtain fully Z-identified ejectile spectra up to Z $lesssim$ 20, with low energy thresholds and large solid-angle coverage. The array is designed in a spherical geometry and consists of 162 triple detector telescopes – 90 covering the angular range 14°-86.5° and 72 covering 93.5° - 166°. Each telescope is composed of (1) a gas-ionization chamber operated at 16 - 18 Torr of C_3F_8 gas; (2) a fully-depleted 500μm ion-implanted silicon detector, and (3) a 28-mm thick CsI (Tℓ) crystal with light guide and photodiode readout. The telescope dynamic range permitted measurement of LCPs and

IMFs with discrete charge resolution over the dynamic range $0.8 \leq$ E/A $\lesssim$ 96 MeV. The silicon/CsI elements also provided isotope identification for ejectiles with kinetic energies E/A > 8 MeV. More specific details of the ISiS detection system and experimental conditions are given in Refs. [25,26].

The calorimetry procedure for determining E*/A follows the same prescription as described in [27,28]. In Fig. 1 we show the correlation between experimental observables and the reconstructed excitation energy. These include total observed charge Z_{obs}, and total thermal kinetic energy, as defined in [25], both of which describe the average excitation energy up to about E*/A = 7-8 MeV.

Examination of the IMF spectra obtained in these studies (Fig. 2) provides evidence for two components, a dominant evaporative-like peak at low energies and a hard exponential tail at fragment energies 20 - 30 MeV above the classical Coulomb barrier [29]. The former resembles equilibrium-like emission from a thermal source. The latter, which is primarily important for the lightest IMFs at forward angles, is associated with fast nonequilibrium/coalescence processes. In order to quantify the average properties of these two mechanisms, we have performed a two-component moving-source analysis of the spectra as a function of excitation energy.

The moving-source analysis has been performed on Z = 3 and 5 - 9 fragments measured at nine angles. Two sources were assumed: a thermal-like source that should be representative of the later stages of the reaction, and a nonequilibrium source that accounts for IMF emission at intermediate times. For Z ≥ 7 a single thermal-like source provides an adequate fit to the data.

Each source was schematically parametrized according to the general relation [29,30]:

$$\frac{d^3\sigma}{d\Omega dE dZ_{IMF}} \propto \ f(Z, \beta, T, p, k_C), \tag{1}$$

where Z is the charge of the source; β is the source velocity (v/c); T is a slope-temperature parameter; p is a spectral shape parameter, and k_C is the fractional Coulomb repulsion energy. A value of $k_C = 1$ represents the Coulomb energy of two nuclei with charge centers

separated by a distance $d = d_0(A_1^{1/3} + A_2^{1/3})$, where d_0 is derived from fission-fragment kinetic-energy systematics [31]. For the residue nuclei of concern in this work, a value of $d_0 \approx 1.80 \pm 0.05$ fm is used, depending on residue mass. This value also gives a good fit to IMF spectra observed in the 200-MeV ^{4}He + ^{197}Au [32] and 280-MeV ^{14}N + ^{197}Au [33] reactions. The parameter p accounts for fluctuations in the Coulomb barrier due to shape distortions of the emitting residue. For the nonequilibrium source a value of p = 0.1 was used, which effectively yields a Maxwellian spectrum, and Eq. (2) is multiplied by a function $e^{-b\theta}$ to account for the forward peaking of the angular distributions [29,33,34].

The spectral function was based on the scission-point statistical emission model of Moretto [30]. The emission probability is given by

$$P(E) = N\left[(2E' - p)e^{-E'/T} erf\{\frac{p - 2E'}{2\sqrt{pT}}\} + 2\sqrt{\frac{pT}{\pi}} exp[\frac{-p^2 + 4E'^2}{4pT}\right] \quad (2)$$

where E′ is the IMF kinetic energy minus the Coulomb barrier energy, corrected for recoil energy, in the source reference frame.

An important aspect of the fitting procedure is that the charge of the emitting source is taken as

$$Z_{source} = Z_{target} + Z_{beam} + Z_{IMF} - Z_{obs}, \quad (3)$$

where Z_{obs} is the total charge observed in the reaction, corrected for solid-angle effects. That is, *it is assumed that all charge in an event is emitted prior to the fragment in question, Z_{IMF}.* While this is an extreme assumption, it reduces the source charge and serves to minimize the Coulomb repulsion energy between the source and IMF,

$$E_C^\circ = 1.44 Z_{IMF}(Z_{source} - Z_{IMF}) \,/ d_o[(A_{source} - A_{IMF})^{1/3} + A_{IMF}^{1/3}], \quad (4)$$

and

$$k_C = E_c(exp)/E_C^\circ, \quad (5)$$

where E_C(exp) is the experimentally-observed Coulomb barrier fit parameter.

Thus, one obtains an *upper limit* for the equilibrium Coulomb parameter values k_C obtained in the fits. This has an important consequence relevant to the question of the breakup density in that it yields a *minimum* value of the breakup separation distance, and hence a *maximum* value of the radial breakup density relative to normal density, ρ/ρ_0.

Representative spectra for carbon fragments observed at 43° and 137° are shown in Fig. 2 for the 4.8 GeV ^{3}He + ^{197}Au reaction for several excitation-energy bins. Fit parameters for these spectra as a function of E*/A are tabulated in [35].

In the following section we examine the implications of the moving-source parameters relevant to fragmentation phenomena. The results of the 4.8 GeV ^{3}He + ^{197}Au reaction will be stressed for this purpose, since the quality of the spectra as a function of angle (especially the Coulomb-peak region) yields the most reliable fits. Typical χ^2/degree of freedom values of 1 - 3 were obtained for the exclusive spectra. Despite the low ISiS thresholds, the spectra from the ^{nat}Ag target lead to greater ambiguities in the fit parameters due to the lower energy of the Coulomb peak and the large yield of very low energy IMFs for high multiplicity events. This leads to increased uncertainties in the Coulomb parameters that makes the fits imprecise. Errors were computed assuming a five percent systematic uncertainty in k_C, added in quadrature to the statistical deviations between different Z_{IMF} values. For the 1.8 GeV ^{3}He + ^{197}Au reaction, inadequate statistics were obtained to perform an analysis for individual IMFs gated on excitation energy.

III. MOVING-SOURCE PARAMETERS

1. Thermal-like source

The most striking feature of IMF emission in these reactions is found in the low energy region of the IMF spectra, where the Coulomb peaks are systematically shifted to energies below those found at low excitation energies, as apparent in Fig. 2. Such behavior is suggestive of emission from the reduced Coulomb field of an expanded/dilute source. This was first pointed out for inclusive spectra by Poskanzer *et al.* [36] and later shown to increase

systematically as a function of deposition energy by Yennello *et al.* [14]. In the top frame of Fig. 3, the average fit values of the Coulomb parameter $< k_C >$ for Z = 3, 5-9 are plotted as a function of E*/A bins.

For the lowest E*/A bin, which should represent IMF emission at relatively low excitation energies, a value of $< k_C > = 0.95 \pm 0.05$ is found. This is nearly identical to the average Coulomb parameters relative to fission obtained from the analysis of the E/A = 20 and 30 MeV reactions [33], as well as the 200-MeV ^{4}He + ^{197}Au data [32], where it is expected that IMF emission occurs from a source near normal nuclear matter density,i.e., $k_C = 1.00$ and $\rho/\rho_0 = 1$. As E*/A increases, k_C decreases with excitation energy up to E/A $\approx$ 5 MeV and then is constant at higher excitation energies. The observed decrease in $< k_C >$ with increasing E*/A serves to reinforce the notion that multifragmentation occurs from an expanded/dilute source. Since we have employed a minimum source charge in the fission systematics, the plotted values of $< k_C >$ should represent upper limits.

Consistent with the results of [32] and [33], we assume that for the lowest energy bin, E*/A = 1.8 MeV, the source is at normal density. This bin is normalized to $\rho/\rho_0 = 1$ and the corresponding average densities at higher E*/A values are calculated under the assumption that the breakup volume $V \propto d^3$ and $d \propto 1/k_C$ (see Eqs. 3 and 4). This establishes the density scale in the bottom frame of Fig. 3. The resulting dependence of ρ/ρ_0 on E*/A shows a systematic decrease in density to $\rho/\rho_0 \lesssim 1/3$ in the vicinity of E*/A = 5-6 MeV, followed by a relatively constant value for higher E*/A bins. Thus, the density vs. E*/A profile obtained in this analysis is consistent with breakup densities predicted by theoretical models of multifragmentation [37–39]. It also corresponds to conclusions about the breakup volume obtained from large-angle IMF-IMF correlation studies [19,40]. Of broader significance, it is important to note that the rapid decrease in ρ/ρ_0 in the region E*/A = 2-5 MeV occurs in the same excitation-energy range where numerous experimental observables – e.g., the IMF multiplicity, charge and isotopic distributions – are changing rapidly [18]; in particular, the time scale becomes very short [19].

Another important result of the moving-source analysis is found in the low average

longitudinal source velocities, as shown in the top frame of Fig. 4. From an experimental point of view, these low source velocities permit observation of the disassembly process with minimum kinematic distortion of the fragment kinetic energy spectra. Low source velocities are particularly important for backward-angle measurements of the low-energy portion of the IMF spectra, which appear to carry the clearest signature of expansion/dilution. The values of $< \beta_{||} >$ in Fig. 4 are in good agreement with multiplicity-dependent rapidity analysis of these data [24] and are relatively insensitive to the Coulomb parameter k_C. Values of $< \beta_{||} >$ are plotted versus E*/A in Fig. 4 for the 4.8 GeV ^{3}He + ^{197}Au system. Similar results are observed for the ^{nat}Ag target at all three energies.

For both targets an initial increase is observed in $< \beta_{||} >$ up to E*/A $\approx$ 5 - 6.0 MeV, after which the average source velocity begins to decrease. The turnover coincides with approximately the same region where the onset of significant expansion/dilution appears in Fig. 3. The decrease in $\beta_{||}$ above E*/A $\tilde{>}$ 6 MeV may be due to the backward recoil effect associated with prompt, forward-peaked emissions, combined with the averaging effect of multifragmentation events. Further, event reconstruction of the data [27] indicates that excitation energies up to E* $\approx$ 1.5 GeV for ^{197}Au and E* $\approx$ 1.0 GeV for ^{nat}Ag are reached for the highest deposition energy collisions. The low values of $\beta_{||}$ suggest that we are forming very highly excited, slowly-moving residues that subsequently undergo multifragmentation breakup. The conversion of projectile kinetic energy into internal excitation energy must occur via multiple N-N scattering and the excitation of Δ and higher resonances [15,41], producing secondaries with a significant transverse momentum component. For the highest excitation energy events, this energy dissipation process imparts a velocity component to the heavy residue that is directed perpendicular to the beam axis, with a corresponding reduction in the longitudinal component, as shown by intranuclear cascade calculations for similar results for GeV proton-induced reactions [42].

The average spectral slope-temperature parameters $< T_{eq} >$ for the thermal-like source are plotted in the bottom panel of Fig. 4 as a function of E*/A for the ^{197}Au target. The average slope temperature increases linearly as a function of excitation energy, as is also

the case for the ^{nat}Ag target. Similar behavior has been shown for the 8.0 GeV/c π^- + ^{197}Au reactions [17]. The results for the lowest excitation-energy bins are in agreement with slope temperature parameters obtained in ^{14}N + ^{nat}Ag and ^{197}Au reactions [33]. For the ^{14}N data at E/A = 100 MeV bombarding energy, similar moving-source fits yield values for the thermal-like component of $< T > \approx$ 7 MeV for ^{nat}Ag and $< T > \approx$ 5.5 MeV for ^{197}Au. This result is consistent with evaporative emission and corresponds well with other results obtained at similar low E*/A values [43,44], suggesting that these results are consistent with emission from a moderately-excited nucleus at normal density.

For the most violent collisions, slope temperatures of up to $< T > \sim$ 15 - 16 MeV are obtained, in agreement with moving-source fits to the spectra of central collisions for the 4.0 GeV ^{36}Ar + ^{197}Au [45] and 8.0 GeV/c π^- + ^{197}Au reactions [17]. However, uncertainties about the degree of equilibration complicate attempts to associate the slope temperatures with the actual thermal properties of the fragmenting source. Further, if the emission is time-dependent, as predicted by the EES model of Friedman [38], then fragments emitted early in the cooling stage will be more energetic than those emitted in the later stages. Thus the slope of the composite spectrum would not represent a true thermodynamic temperature.

In these fits the amplification parameter p is introduced primarily as a fitting parameter to account for the broadening of the Coulomb-like spectral peaks. As has been shown previously [33], this parameter increases with IMF charge and is slightly larger for the ^{197}Au target than for ^{nat}Ag.

2. Nonequilibrium source

The fast/nonequilibrium source employed in the fitting procedure is necessary to account for the energetic tail of the IMF spectrum. These fragments are presumably emitted during the early stages of the reaction dynamics and are observed in all nuclear reaction studies well above the Coulomb barrier [10]. Various mechanisms have been proposed to account for formation of these complex ejectiles, for example coalescence and preequilibrium emission, but the process remains poorly understood. As mentioned in Sec II, in the absence of a better

knowledge of the emission mechanism, we have employed Eq. (2) with p = 0.1 (which is essentially a Maxwellian kinetic energy distribution) to describe these fragments, consistent with earlier analyses [27,33,46]. To account for the forward emission of the fragments, an angular distribution function $e^{-b\theta}$ is included in Eq. (2).

The fast source is primarily important for Z = 3-6 fragments and excitation energies $E^*/A \lesssim 5$ MeV. Li fragments dominate the fast-source yield, comprising about 15% of total Li production for the Ag target and 25% for Au. For carbon fragments the fast source contributes only about 5% to the total yield from Ag and $< 10\%$ for Au. For fragments heavier than carbon, the fits require only the slow source.

The fast-source fitting parameters for $\beta_{||}, k_C$, and T, do not exhibit any significant trends as a function of beam energy, target, IMF charge or excitation energy. Thus, this component appears somewhat universal in its behavior. The two most relevant parameters in the fitting procedure are the fast-source longitudinal velocity, β_2, and the slope temperature parameter, T_2. The fast-source velocities are about three times greater than those for the slow source, with values ranging from $\beta_2 \sim 0.025$-0.035 for the Ag target and $\beta_2 \sim 0.020$-0.030 for Au. For Li fragments the fast-source velocities are typically 50% larger than for heavier fragments. The slope temperature parameter is nearly identical for all systems; values of $< T_2 > = 19 \pm 2$ MeV for Li satisfy the spectra and for heavier fragments this value is $< T_2 > = 18 \pm 2$ MeV. These fast/nonequilibrium-source temperatures are nearly identical to those found in a similar analysis of IMF spectra from the E/A = 20-100 MeV ^{14}N + Ag, Au reactions [33], suggesting a commonality in their origin.

The fast-source fits are not strongly dependent on the Coulomb parameter. For the gold target, where the spectral peaks are relatively well-defined as a function of excitation energy, values of $k_C \sim 0.2$- 0.3 are obtained. For Ag, the k_C values are closer to unity, but are difficult to constrain due to the lack of definition for the Coulomb-like peak in the data. Finally, the angular distribution parameter, b, which is required to fit heavy-ion data due the strongly forward-peaked nature of the fast source [33], is less pronounced for GeV ^{3}He-induced reactions. This indicates that the nonequilibrium mechanism for producing

the fast IMF component involves significant randomization of the source recoil axis prior to emission.

Thus, the fast source in these reactions appears to be a somewhat universal feature of the collision dynamics for nuclear reactions induced on complex nuclei with intermediate-to-high-energy projectiles. The analysis performed here and in [17] suggests that nonequilibrium emission occurs at a late stage of the fast cascade, but prior to complete randomization of the N-N scattering process that leads to equilibrium.

3. Cross Sections

The moving-source fits have been integrated over all angles and fragment energies to obtain total IMF production cross sections, as well as values for the fast and slow sources. These are listed as a function of IMF charge in Table I and as a function of E*/A in Table II for each reaction studied. The combined effects of statistical and systematic errors are estimated to be $\pm$ 20%; relative errors are significantly smaller. These cross sections are consistent with values derived in an earlier analysis based on integration of the experimental data, which included extrapolated yields due to missing-angle and detector energy thresholds [24].

In Table I the elemental cross sections are listed for the slow, fast and total IMF yields. Between 1.8 and 4.8 GeV there is a significant increase in the cross sections for both reactions. The similar yields for the 3.6 and 4.8 GeV bombardments of ^{nat}Ag have been attributed to a saturation of excitation-energy deposition that sets in near 3.6 GeV [25]. Consistent with other studies [10–15], the elemental cross sections are dominated by Li fragments for both the fast and slow sources, with the yields decreasing approximately as a power law, $\sigma(Z) \propto Z^{-\tau}$. Relative to the fast source, the yield distributions decrease much more slowly for the slow source; i.e., low values of τ, or a preference for larger fragment size. For the slow source values of τ range from $\tau \sim$ 1.5-2.0, with a minimum near E*/A $\sim$ 6-7 MeV, as observed in hadron-induced reactions on ^{197}Au [18]. The fast source is important primarily for the lightest fragments (Z $\lesssim$ 6), with τ values in the $\tau \sim$ 2.5-3.5 range.

Table II lists the slow, fast and total IMF cross sections as a function of excitation energy.

Statistics precluded an E*/A-dependent analysis of the 1.8 GeV ^{3}He + ^{197}Au reaction. Effects of geometric corrections to the data to account for the ISiS acceptance are discussed in [28]. In the interpretation of Table II it must be kept in mind that the probability for excitation energy deposition decreases strongly with increasing E*/A [25]. For example, less than 5% of the reaction cross section leads to residues with E*/A $>$ 5.0 MeV, so that when weighted by the fraction of the reaction cross section for each E*/A bin, the relative IMF cross sections increase significantly as the excitation energy increases. The bombarding-energy dependence is reflected in the ^{nat}Ag data. For E*/A $<$ 5.0 MeV, there is only a slight increase in the IMF cross section, from 153 mb at 1.8 GeV to about 200 mb for the 3.6 and 4.8 GeV ^{3}He beams. In contrast, between 1.8 and 4.8 GeV the IMF cross section for the slow source with E*/A $>$5.1 MeV increases from 32 to 140 mb. The target effect is also strong. At 4.8 GeV bombarding energy the thermal cross section for E* $\tilde{>}$ 5 MeV events is 140 mb for the Ag target compared with 376 mb for Au. When corrected for multiplicity effects, it is estimated that about 5% of the total reaction cross section results from multifragmentation. Overall, the slow-source IMF yield dominates that for the fast source for all E*/A bins. The fast source is most important for low values of excitation energy, which presumably are associated with more peripheral impact parameters.

IV. ISOTOPE YIELD RATIOS

Isotope yield ratios for H and He ejectiles have also been investigated for the 4.8 GeV ^{3}He bombardments of Ag and Au. We examine the H and He isotope ratios as a function of target, beam energy, emission angle and E*/A. Double ratios of these data are then used to calculate the nuclear temperature for the 4.8 GeV ^{3}He + ^{nat}Ag, ^{197}Au systems, based on the approach of Albergo [49].

Figure 5 presents total deuteron-proton yield ratios as a function of E*/A for the 4.8 GeV ^{3}He + Au reaction at a forward and backward angle. The ^{3}He + Ag system behaves similarly. The left panel has no IMF gating requirement whereas the right panel presents

the ratios with the gating condition of at least one IMF being detected. For both gating conditions and angles, the deuteron-to-proton ratios increase with up to $E^*/A \sim 4$ MeV and then become relatively constant beyond this excitation energy. When correlated with the arguments concerning density, this result suggests that the d/p ratio is frozen in for $\rho/\rho_0 \lesssim 0.3$. The ratios determined by backward-angle detectors are consistently lower than those at forward angles, most likely due to the difficulty in isolating thermal and non-thermal particles. For both forward and backward angles the ratios converge to a nearly constant value of about 0.5 - 0.6 at high excitation energy; the ratios do not appear to be significantly affected when the IMF gating condition is imposed.

Figure 6 presents the total deuteron-to-proton and the triton-to-proton yield ratios at 137° as a function of E^*/A for 4.8 GeV ^{3}He reactions with gold and silver targets. The side-by-side comparison of the two targets shows the qualitative similarity in the ratios as a function of increasing excitation energy. Also readily apparent are the larger ratios achieved in the gold system. The triton-to-proton ratios flatten out at values of about 0.28 and 0.45 for the silver and gold systems, respectively. A comparison of maximum values between silver and gold shows the difference is greater for the triton-to-proton ratios than for the deuteron-to-proton ratios. This result most likely reflects the difference in N/Z ratios of the silver and gold targets, which are 1.3 and 1.5, respectively. As with the d/p ratios, the t/p ratios show a distinct slope change near $E^*/A \approx 4$ MeV.

The ^{3}He-to-^{4}He total yield ratios are presented in Fig. 7 as a function of the excitation energy for 4.8 GeV ^{3}He on gold and silver targets at two angles, 43 and 137 degrees. The forward-angle ratios for both targets show an initial sharp decrease in the ^{3}He/^{4}He values with increasing excitation energy, which can be attributed to the strong non-thermal ^{3}He component of the spectrum at low energies. With increasing excitation energy, the yields decrease more gradually, more so for the ^{197}Au than for the ^{nat}Ag target. At backward angles, where the yield of non-thermal ^{3}He ions is much lower, the ratios appear to be relatively constant, ^{3}He/^{4}He $\simeq 0.5$ for ^{nat}Ag and 0.3 for Au, perhaps reflecting to some extent that the more neutron-excess composition of the ^{197}Au target favors ^{4}He over ^{3}He

and that the formation of ^{4}He is more favored energetically.

More instructive is the dependence of helium isotope ratios on particle kinetic energy, which has been reported previously [34,47,48]. The strong, nearly linear change in the ^{3}He-^{4}He ratios as a function of fragment kinetic energy is shown in Fig. 8 for both silver and gold targets at a bombarding energy of 4.8 GeV. The slope for both targets is the same but differs slightly with detector angle. At low kinetic energies, where the Q-value is an important constraint on the emission probability, ^{4}He dominates the yields. At higher energies Q-values diminish in importance, and ^{3}He becomes dominant. This change in the ^{3}He/^{4}He ratio illustrates the transition from equilibrium-dominated emission to preequilibrium-dominated emission. From Fig. 8 it is clear that isotope ratios are sensitive to the kinetic energy acceptance of the detection system, and that low energy non-equilibrium ejectiles cannot be uniquely separated from energetic equilibrium emissions.

In evaluation of source temperatures from isotope-yield ratios [22,49] , detector energy and angle acceptance are important variables, since the isotope ratios for a given element are sensitive to the fragment energy spectrum [17]. For the analyses here we have chosen only H and He ejectiles that fall in the "thermal" part of the kinetic energy spectrum as defined in [25]. The experimental constraint of isotope-dependent particle-identification thresholds limited the acceptance to kinetic energies with E/A $>$ 8 MeV. In order to be self-consistent, for hydrogen isotopes the acceptance range was 15-25 MeV and for He ions acceptance was 38-52 MeV, which adjusts the H and He yields for Coulomb-barrier differences.

Using the average thermal-like excitation energies and residue masses from the reconstructed data [27,28,49,50], we have determined the E*/A versus T heating curve for the ^{nat}Ag and ^{197}Au reactions in Fig. 9. Here the temperatures T corresponding to a given excitation energy per nucleon have been derived from the double-isotope-ratio method [49] using the yield ratio Y = (^{2}H/^{3}H)/(^{3}He/^{4}He) isotope ratios described above, measured at backward angles (137 degrees) to minimize preequilibrium effects. Only thermal-like H and He isotopes were considered in the calculation of T and the correction factor for contributions due to sequential decay [51] are negligible for this isotope set ($\Delta T \lesssim 0.3$ MeV).

Also included in this plot is a low-energy inclusive point from the 180-MeV ^{4}He + ^{116,124}Sn systems, derived from a large set of IMF isotope ratios [52].

The heating curve increases rapidly at low E*/A, exhibits a distinct slope change near 2-3 MeV/nucleon, and then shows a gradual increase up to E*/A $\approx$ 8 MeV. Our results for these very asymmetric systems are generally consistent with those observed in other studies [17,22,53–55]. However, both ^{nat}Ag and ^{197}Au residues yield essentially identical results, which varies somewhat from the recent analysis of caloric curves as a function of residue mass, indicating that the Ag data should be somewhat higher than that for Au [53]. This may be in part due to threshold effects in the analysis of the presnet data. Also shown in Fig. 9 is the behavior expected for a simple Fermi gas with level-density parameter a = A/11 MeV^{-1}, and predictions based on the expanding emitting source (EES) model of Friedman [38] and the statistical multifragmentation (SMM) model of Botvina [56]. Initial residue excitation-energy, mass and charge distributions were taken from INC calculations [57]. In each calculation the dashed line gives the full model prediction and the solid line shows the effect when energy cuts are imposed on the H and He spectra that correspond to the ISiS detector threshold for isotope identification ($\sim$ 30 MeV). The $\sim$ 1 MeV temperature difference above the full model curve and other results [22,53,55] is a consequence of the strong dependence of the ^{3}He/^{4}He ratio on the He kinetic energy and the energy thresholds for ISiS, discussed in greater detail in [17].

V. SUMMARY

Data from reactions between 1.8-4.8 GeV ^{3}He ions with ^{nat}Ag and ^{197}Au target nuclei have been analyzed in the framework of a two-component, moving-source model, assuming thermal-like and nonequilibrium sources. This approach provides a systematic description of fragment spectra, angular distributions and cross sections as a function of E*/A.

The major fraction of the IMF yield can be accounted for by emission from an equilibrium-like source. The most striking result of the fits is found in the dependence of

the Coulomb barrier parameters on excitation energy for the 4.8 GeV ^{3}He + ^{197}Au system. For the lowest E*/A bin, this parameter is consistent with similar values obtained in lower energy light- and heavy-ion reactions and fission kinetic-energy systematics [32,33]. With increasing E*/A, the barrier parameter decreases monotonically and then become constant for E*/A $\gtrsim$ 5 MeV. When translated into nuclear breakup radii, these parameters imply a nuclear radius that is about 50% larger than normal nuclear matter, or a breakup density of $\rho/\rho_o \sim 1/3$, consistent with theoretical models of multifragmentation. The average slope-temperature parameters increase from T $\approx$ 6 MeV for low deposition energies to T $\approx$ 16 MeV for the most highly excited systems. Finally, the average source-velocity parameters initially increase to a maximum of $\beta \sim 0.016$ for E*/A $\lesssim$ 5 MeV and then decrease to $\beta \sim$ 0.010 for the highest deposition energy events. This implies significant transverse momentum transfer in the collision stage in order to achieve deposition energies up to E* $\sim$ 1.0 - 1.5 GeV.

The nonequilibrium source is most important for light IMFs with Z $\leq$ 6. It comprises about 15% of the total IMF yield for reactions on the Ag target and 25% for the Au target. There is little sensitivity of the fast-source fit parameters to beam energy or deposition energy. The fast source velocities are about three times greater than for the slow source. Rather uniform slope temperatures are observed, T $\sim$ 18-20 MeV. These values are nearly identical to fast source fits to heavy-ion data.

Examination of the ^{1}H: ^{2}H: ^{3}H: and ^{3}He: ^{4}He isotope ratios shows an increasing probability for the emission of neutron-excess isotopes as the excitation energy increases up to E*/A $\sim$ 5 MeV and is nearly constant thereafter. The strong dependence of the ^{3}He/^{4}He ratio on He kinetic energy is pointed out, emphasizing the importance of detector acceptance in calculating isotope ratio temperatures and the need to minimize prequilibrium particles from such analyses. The caloric curve results are in approximate agreement with other data [50], as well as with both EES and SMM models, both of which assume a phase transition. The data are about 1 MeV higher than the model predictions due to the strong sensitivity of He isotope ratios (hence temperature) on fragment kinetic energy. This may be evidence

for a "cooling" effect [17,59].

The most significant impact of the present work emerges when the derived breakup densities are compared with the isotope-ratio temperatures as a function of excitation energy. In the interval E^*/A = 2-5 MeV, the density decreases from normal nuclear density to a near-constant value of $\rho/\rho_0 \lesssim 0.3$ at $E^*/A \simeq 5$ MeV and above. Over this same E^*/A range the temperature versus E^*/A (caloric) curve deviates from Fermi gas behavior and becomes nearly flat. This correlation supports a scenario in which a nuclear liquid-gas phase transition is driven by Coulomb instabilities that develop when the nuclear density approaches $\rho/\rho_0 \sim 0.3$, as previously suggested by Natowitz [21].

This work was supported by the US Department of Energy and National Science Foundation, CEA Saclay, France, the National Research Council of Canada and KBN grant no. 0719/P3/93/04 (Poland). We also acknowledge the technical staff of DAPNIA/CEA Saclay and the operations staff of LNS for their support in making these experiments possible.

REFERENCES

[1] K. Kwiatkowski *et al.*, Phys. Rev. Lett. **74**, 3756 (1995).

[2] V. Lipps *et al.*, Phys. Rev. Lett. **72**, 1604 (1994).

[3] L. Pienkowski *et al.*, Phys. Lett. B **336**, 147 (1994).

[4] G. Wang, K. Kwiatkowski, V.E. Viola, W. Bauer and P. Danielewicz, Phys. Rev. C. **53**, 1811 (1996).

[5] G. Friedlander *et al.*, Phys. Rev. Lett. **94**, 727 (1954); R. Wolfgang *et al.*, Phys. Rev.**103**, 394 (1956).

[6] N.A. Perfilov *et al.*, Soviet Phys. Usp. **3**, 1 (1960).

[7] V.P. Crespo *et al.*, Phys. Rev. **131**, 1765 (1963); R.G. Korteling and E.K. Hyde, Phys. Rev. **136**, 425 (1964).

[8] J. Hudis, in Nuclear Chemistry, (Academic Press, New York, ed. L. Yaffe), p. 169 (1968).

[9] J. Hüfner, Physics Reports **125**, 130 (1985).

[10] W.G. Lynch, Ann. Rev. Nucl. Sci. **37**, 493 (1987).

[11] A.I. Warwick *et al.*, Phys. Rev. C **27**, 1083 (1983).

[12] J.E. Finn *et al.*, Phys. Rev. Lett. **49**, 1321 (1982).

[13] S.J. Yennello *et al.*, Phys. Lett. B **246**, 26 (1990).

[14] S.J. Yennello *et al.*, Phys. Rev. C **48**, 1092 (1993).

[15] K. Kwiatkowski *et al.*, Phys. Rev. C **49**, 1516 (1994).

[16] S. Turbide, L. Beaulieu, P. Danielewicz and V.E. Viola *et al.*, unpublished.

[17] A. Ruangma *et al.*, Phys. Rev. C **66**,044603 (2002).

[18] L. Beaulieu *et al.*, Phys. Rev. C **63**, 031302R (2001).

[19] L. Beaulieu *et al.*, Phys. Rev. Lett. **84** 5971 (2000).

[20] G. Wang *et al.*, Phys. Rev. C **57** R2786 (1998).

[21] J.B. Natowitz *et al.*, Phys. Rev C **65**, 034618 (2002); Phys. Rev. C **66**, 031601R (2002).

[22] J. Pochodzalla *et al.*, Phys. Rev. Lett. **75**, 1040 (1995).

[23] J.B. Natowitz, K. Hagel, M. Murray, L. Qin, R. Wada and J. Wang, Phys. Rev Lett. **89**, 212701 (2002).

[24] E. Renshaw Foxford *et al.*, Phys. Rev. C **54**, 749 (1996).

[25] K.B. Morley *et al.*, Phys. Rev. C **54**, 737 (1996).

[26] K. Kwiatkowski *et al.*, Nucl. Instr. Meth. A **360**, 571 (1995).

[27] K. Kwiatkowski *et al.*, Phys. Lett B **423**, 21 (1998)

[28] T. Lefort *et al.*, Phys. Rev. C **64**, 064603 (2001).

[29] K. Kwiatkowski, J. Bashkin, H. Karwowski, M. Fatyga and V.E. Viola Phys. Lett. B **171**, 41 (1986).

[30] L.G. Moretto, Nucl. Phys. A **247**, 211 (1975).

[31] V.E. Viola, K. Kwiatkowski and M. Walker, Phys. Rev. C **31**, 706 (1985).

[32] J. Zhang, K. Kwiatkowski, D. Bonser, M. Fatyga, S.D. Coon, K. Stith, V.E. Viola, L.W. Woo and S.J. Yennello, Phys. Rev. C. **56**, 1918 (1997).

[33] J.L. Wile *et al.*, Phys. Rev. C **45**, 2300 (1992).

[34] J.R. Wu, C.C. Chang and H.D. Holmgren, Phys. Rev. C **19**, 370, 659, 698 (1979).

[35] D.S. Bracken, Ph.D. Thesis, Indiana University 1996.

[36] A.M. Poskanzer *et. al.*, Phys. Rev. C **3**, 1759 (1971).

[37] J. Bondorf *et al.*, Nucl. Phys. A **443**, 321 (1985); **436**, 265 (1985).

[38] W.A. Friedman, Phys. Rev. C **42**, 667 (1990).

[39] D.H.E. Gross, Rep. Prog. Phys. **53**, 605 (1990); Phys. Lett. B **318**, 405 (1990).

[40] G. Wang *et al.*, Phys. Rev. Lett. **343**, 270 (1997).

[41] J. Cugnon *et al.*, Nucl. Phys. A **379**, 533 (1982); **462**, 751 (1987).

[42] W.-c. Hsi *et al.*, Phys. Rev. C **60**, 034609 (1999).

[43] F. Goldenbaum *et al*, Phys. Rev. Lett. **77**, 1230 (1996).

[44] U. Jahnke *et al.*, Phys. Rev. Lett. **83** 4959 (1999).

[45] L. Phair *et al.*, Ph.D. Thesis, Michigan State University, 1993.

[46] G.D. Westfall *et al.*, Phys. Rev. C **17**, 1368 (1978).

[47] J. Gosset *et al.*, Phys. Rev. C **16**, 629 (1977).

[48] W. Skulski *et al.*, Phys. Rev. C **40**, 1279 (1989).

[49] S. Albergo, Nuovo Cimento **89A**, 1 (1985).

[50] J. Brzychczyk, unpublished results.

[51] M.B. Tsang *et al.*, Phys. Rev. Lett. **78**, 3836 (1997).

[52] J. Brzychczyk *et al.* Phys. Rev. C **47**, 1553 (1993).

[53] J.B. Natowitz *et al.*, Phys. Rev. C **52**, R2322 (1995); R. Wada *et al.*, Phys. Rev. C **55**, 227 (1997).

[54] J.A. Hauger *et al.*, Phys. Rev. Lett. **77**, 235 (1996).

[55] Y.G. Ma *et al.*, Phys. Lett. B **390**, 41 (1997).

[56] A. Botvina *et al.*, Nucl. Phys. A **507**, 649 (1990).

[57] Y. Yariv and Z. Fraenkel, Phys. Rev. C **20**, 2227 (1979); **24**, 488 (1991).

[58] P. Chomaz, AIP Conference Proc.**610**, 167 (2002).

[59] K. Kwiatkowski *et al.*, Nucl. Phys. A **630**, 168c (1998).

FIGURES

FIG. 1. Correlation of E*/A with total observed charge Z_{obs} (left) and total thermal energy (right) for the 4.8 GeV ^{3}He + ^{197}Au reaction.

FIG. 2. Energy spectra at 43° and 137° for carbon fragments emitted from the 4.8 GeV/c ^{3}He + ^{197}Au reaction, as a function of excitation energy. Symbols are $< E*/A >$ = 3.4 MeV (•); 4.6 MeV(□); 5.7 MeV (△); 6.8 MeV (◇) and 7.9 MeV (▽).

FIG. 3. Average Coulomb parameter $< k_C >$ for Z= 3, 5-9 fragments (top) and derived source breakup density $< \rho/\rho_0 >$ (bottom) as a function of E*/A for the 4.8 GeV ^{3}He + ^{197}Au reaction.

FIG. 4. Average longitudinal source velocity $< \beta_{||} >$ (top) and average thermal source slope temperature $< T_{eq} >$ (bottom) as a function of E*/A for the 4.8 GeV ^{3}He + ^{197}Au reaction.

FIG. 5. Plot of deuteron-to-proton ratios as a function of E*/A at laboratory angles of 43° and 137° for the reaction of 4.8 GeV ^{3}He + ^{197}Au. The right panel has the added condition of at least one identified IMF, while the left panel has no IMF gating condition.

FIG. 6. Plot of deuteron-to-proton and triton-to-proton yield ratios as a function of E*/A at a laboratory angle of 137°. The left panel is for the reaction of 4.8 GeV ^{3}He + ^{nat}Ag while the right panel is for the same projectile energy but with a ^{197}Au target.

FIG. 7. Plot of ^{3}He to ^{4}He yield ratios as a function of E*/A at laboratory angles of 43° and 137°. The left panel is for the reaction of 4.8 GeV ^{3}He + ^{nat}Ag while the right panel is for the same projectile energy but with a ^{197}Au target.

FIG. 8. Plot of ^{3}He to ^{4}He ratios as a function of He kinetic energy at laboratory angles of 43° and 137°. The left panel is for the reaction of 4.8 GeV ^{3}He + ^{nat}Ag while the right panel is for the same projectile energy with a ^{197}Au target.

FIG. 9. Isotope-ratio temperature versus reconstructed E*/A for 4.8 GeV ^{3}He + ^{nat}Ag, ^{197}Au reactions. The symbols are identified on the figure: the square is from the ^{4}He + Sn data of Ref. [50]. Left frame compares data with the INC/EES model [38,57] and right frame compares with the INC/SMM model [56,57]. Solid curves are model predictions with experimental cuts imposed on H and He energy spectra. Dashed curves show the effect of removing the experimental cuts. Dotted curves show Fermi gas behavior with a = 11 MeV^{-1}

.

TABLES

TABLE I. Elemental cross sections of IMFs for thermal, nonequilibrium and total source contributions for each system studied in this work.

	σ_{IMF}(mb)						
	Li	B	C	N	O	F	Total
1.8 GeV Ag							
Thermal	98	27	25	15	9.9	6.5	182
Nonequilibrium	15	3	—	—	—	—	18
Total	113	30	25	15	9.9	6.5	200
3.6 GeV Ag							
Thermal	159	48	45	30	22	14	318
Nonequilibrium	31	7	4	—	—	—	42
Total	190	55	49	30	22	14	360
4.8 GeV Ag							
Thermal	154	55	49	32	22	15	341
Nonequilibrium	30	6	3	—	—	—	39
Total	194	61	52	32	22	15	380
1.8 GeV Au							
Thermal	142	31	29	18	14	14	252
Nonequilibrium	109	32	15	12	—	—	168
Total	251	63	44	30	14	14	420
4.8 GeV Au							
Thermal	368	116	161	109	81	60	893
Nonequilibrium	296	86	5	—	—	—	387
Total	664	202	166	109	81	60	1280

TABLE II. Integrated cross sections for thermal, nonequilibrium and total sources as a function of excitation energy. No data are listed for the 1.8 GeV ^{3}He + ^{197}Au system due to inadequate statistics.

E*/A (MeV =	1.0-2.5	2.5-3.9	4.0-5.1	5.2-6.2	6.3-7.4	$\geq$ 7.5	Total
1.8 GeV Ag							
Thermal	13	67	73	22	7.0	2.5	180
Nonequilibrium	1.7	10	5.5	1.3	0.6	0.3	19
Total	15	77	79	24	7.6	2.8	200
3.6 GeV Ag							
Thermal	9.0	82	112	72	33	13	320
Nonequilibrium	1.6	12	13	7.1	4.8	3.6	42
Total	11	94	125	79	38	17	360
4.8 GeV Ag							
Thermal	8.4	75	118	86	42	12	340
Nonequilibrium	1.4	11	13	8.4	6.5	3.3	44
Total	10	86	131	94	49	15	385
4.8 GeV Au							
Thermal	37	214	290	249	98	29	920
Nonequilibrium	31	151	147	13	8.3	5.8	360
Total	68	355	427	262	106	35	1280

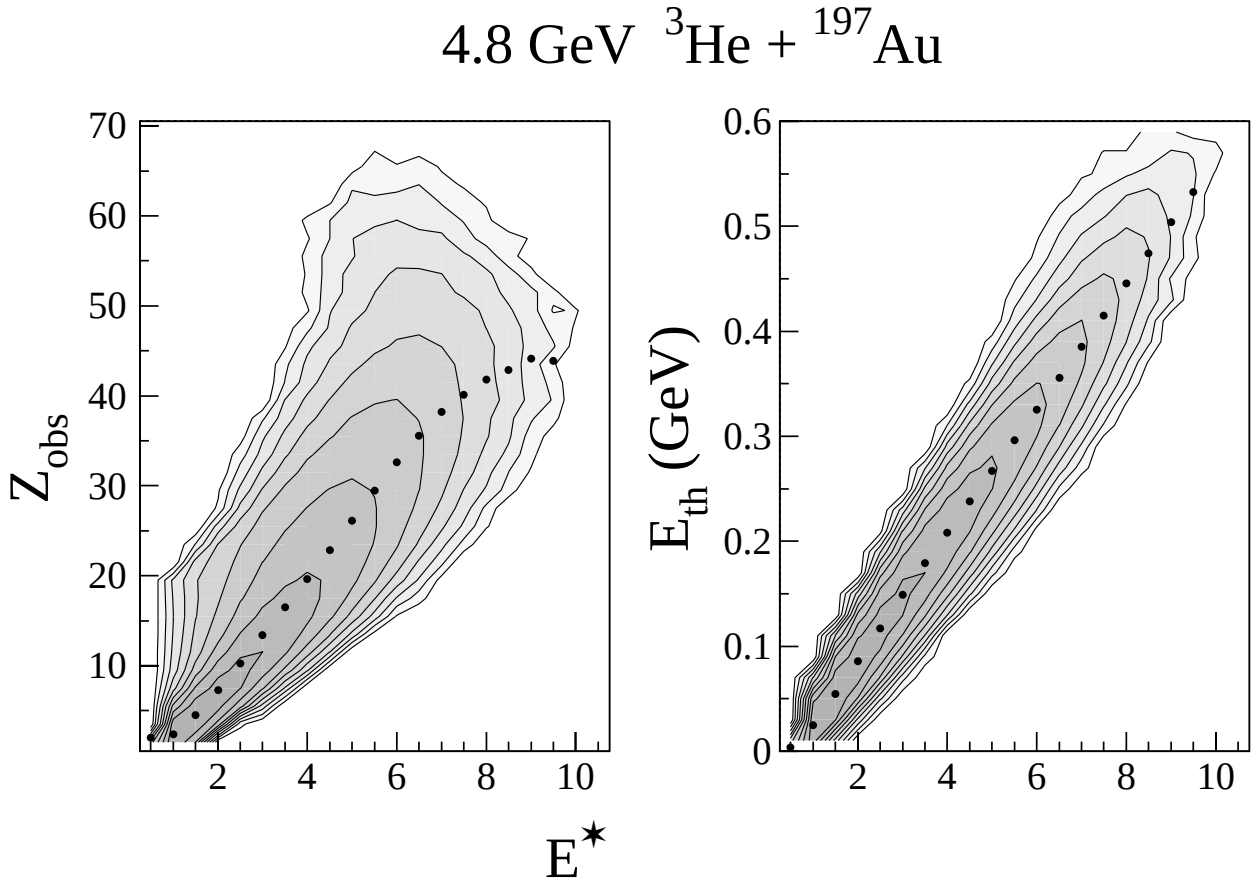
4.8 GeV ^{3}He + ^{197}Au
Z_{obs}
E_{th} (GeV)
$E^{\star}$

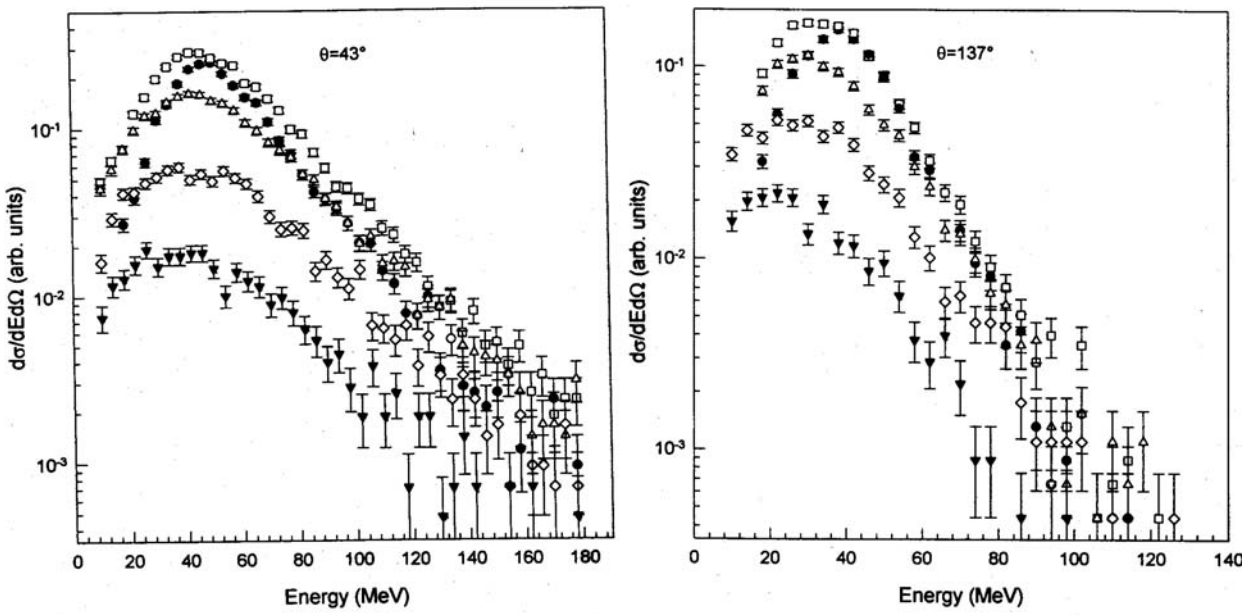
θ=43°
θ=137°
dσ/dEdΩ (arb. units)
Energy (MeV)

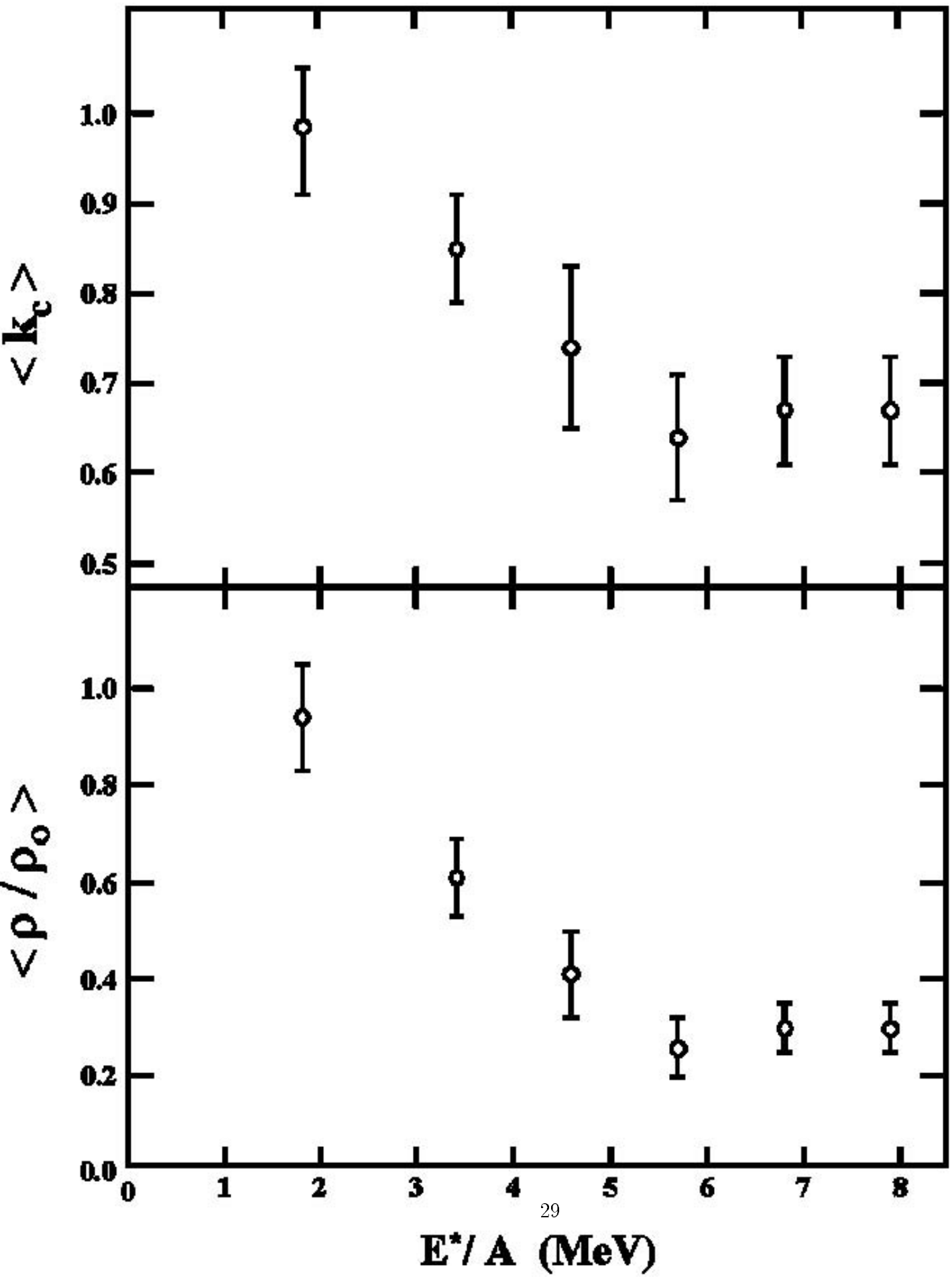
1.0
0.9
0.8
0.7
0.6
0.5
< k_c >
1.0
0.8
0.6
0.4
0.2
0.0
< ρ / ρ_o >
0
1
2
3
4
5
6
7
8
E*/ A (MeV)

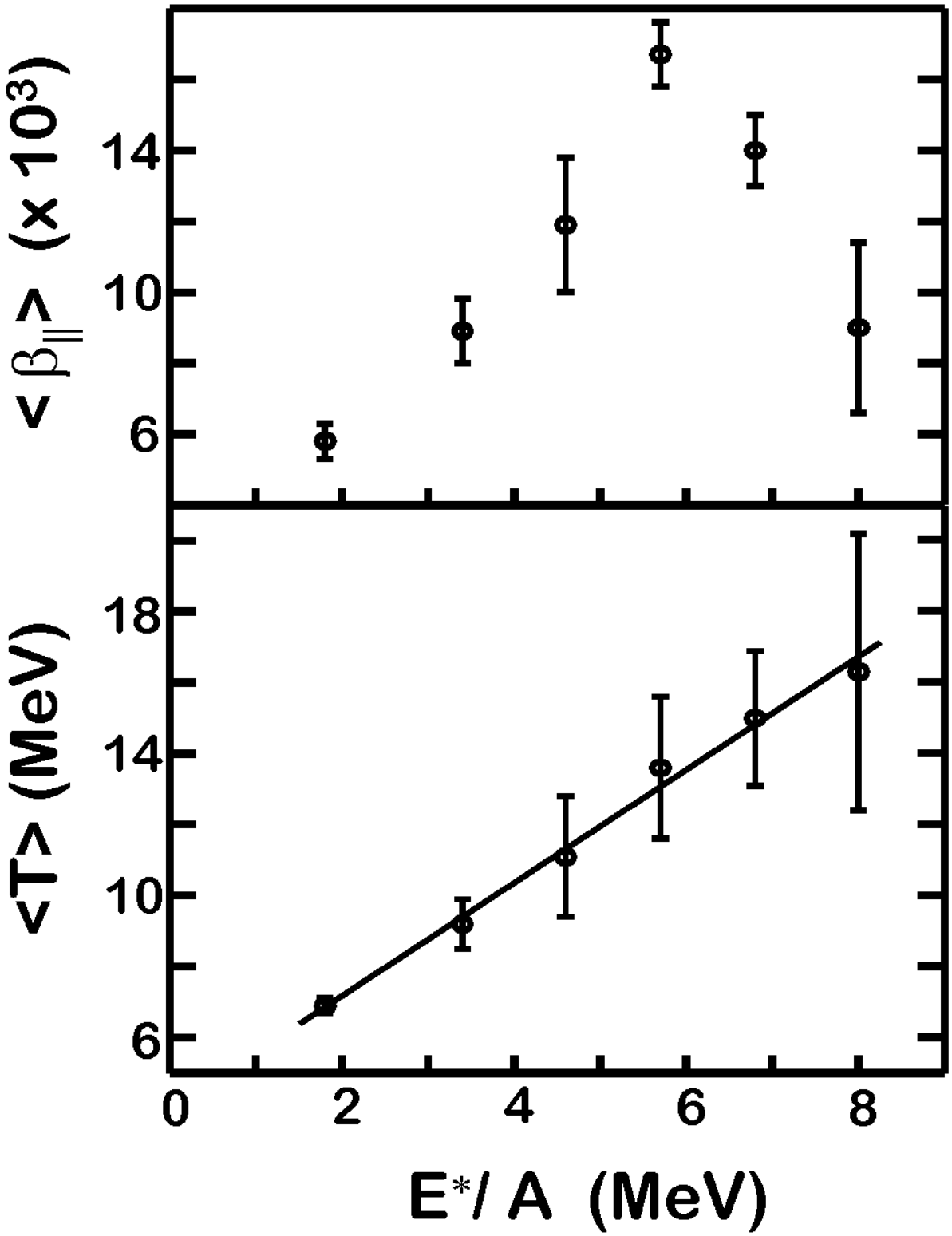
< β|| > (x 10³)
14
10
6
<T> (MeV)
18
14
10
6
0
2
4
6
8
E*/ A (MeV)

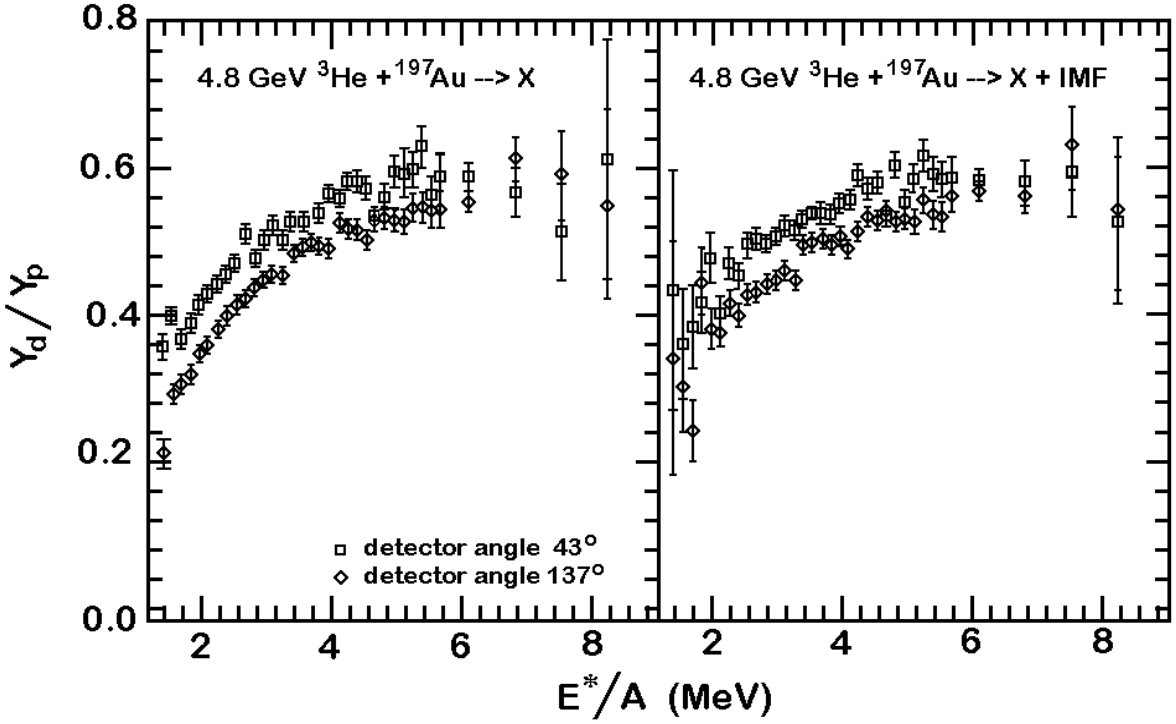
4.8 GeV ^{3}He + ^{197}Au --> X
4.8 GeV ^{3}He + ^{197}Au --> X + IMF
detector angle 43°
detector angle 137°
Y_d / Y_p
E^*/A (MeV)
0.0
0.2
0.4
0.6
0.8
2
4
6
8

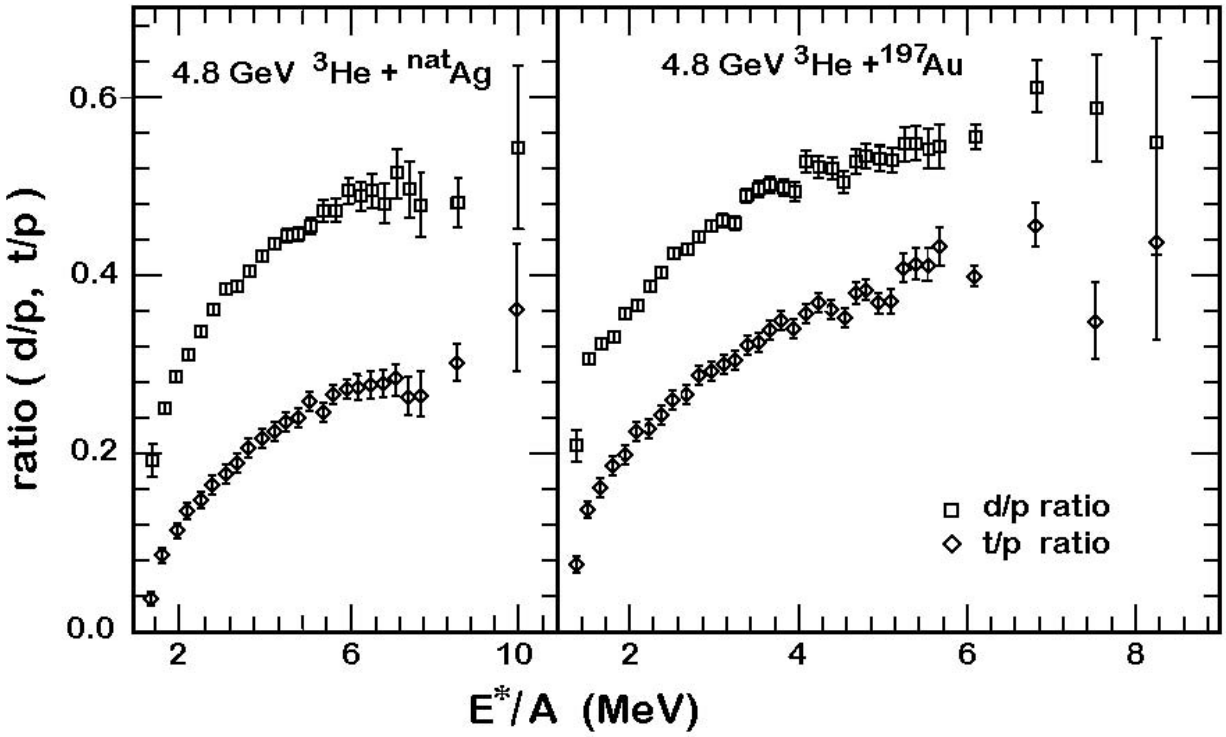
4.8 GeV ^{3}He + ^{nat}Ag
4.8 GeV ^{3}He + ^{197}Au
d/p ratio
t/p ratio
ratio (d/p, t/p)
E*/A (MeV)
0.0
0.2
0.4
0.6
2
6
10
2
4
6
8

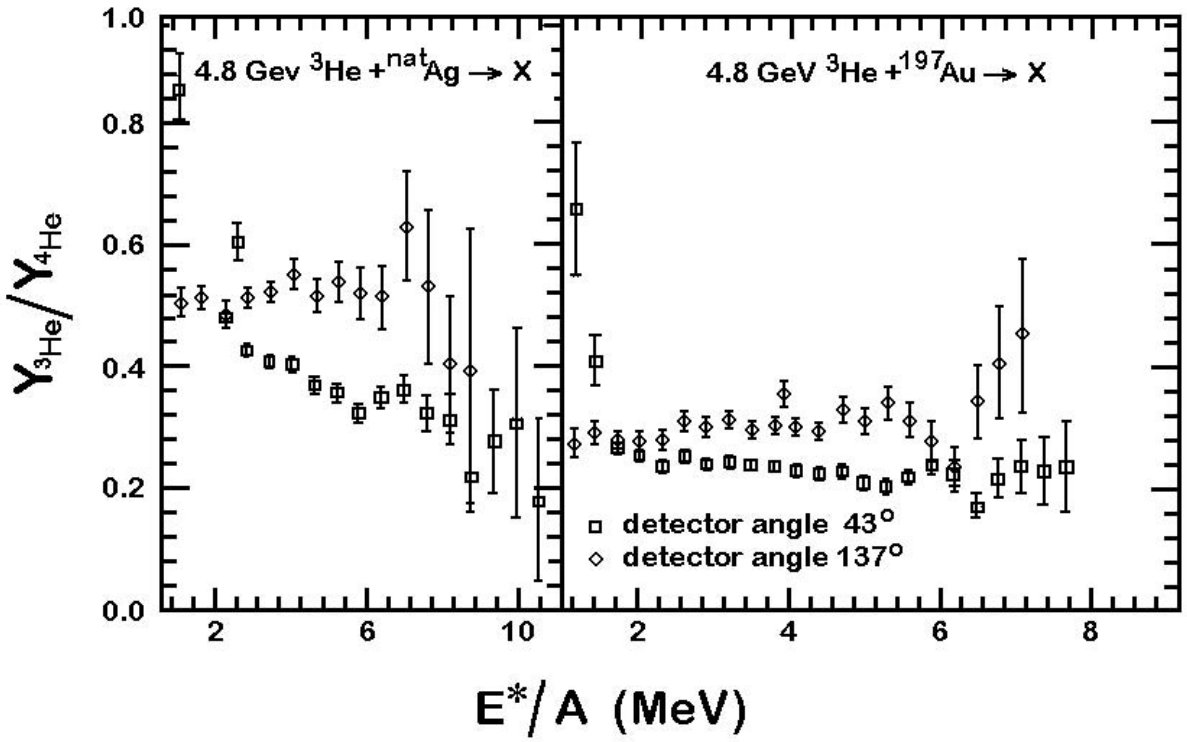
4.8 Gev ^{3}He + ^{nat}Ag → X
4.8 GeV ^{3}He + ^{197}Au → X
detector angle 43°
detector angle 137°
$Y_{^3He}/Y_{^4He}$
E*/A (MeV)
1.0
0.8
0.6
0.4
0.2
0.0
2
6
10
2
4
6
8

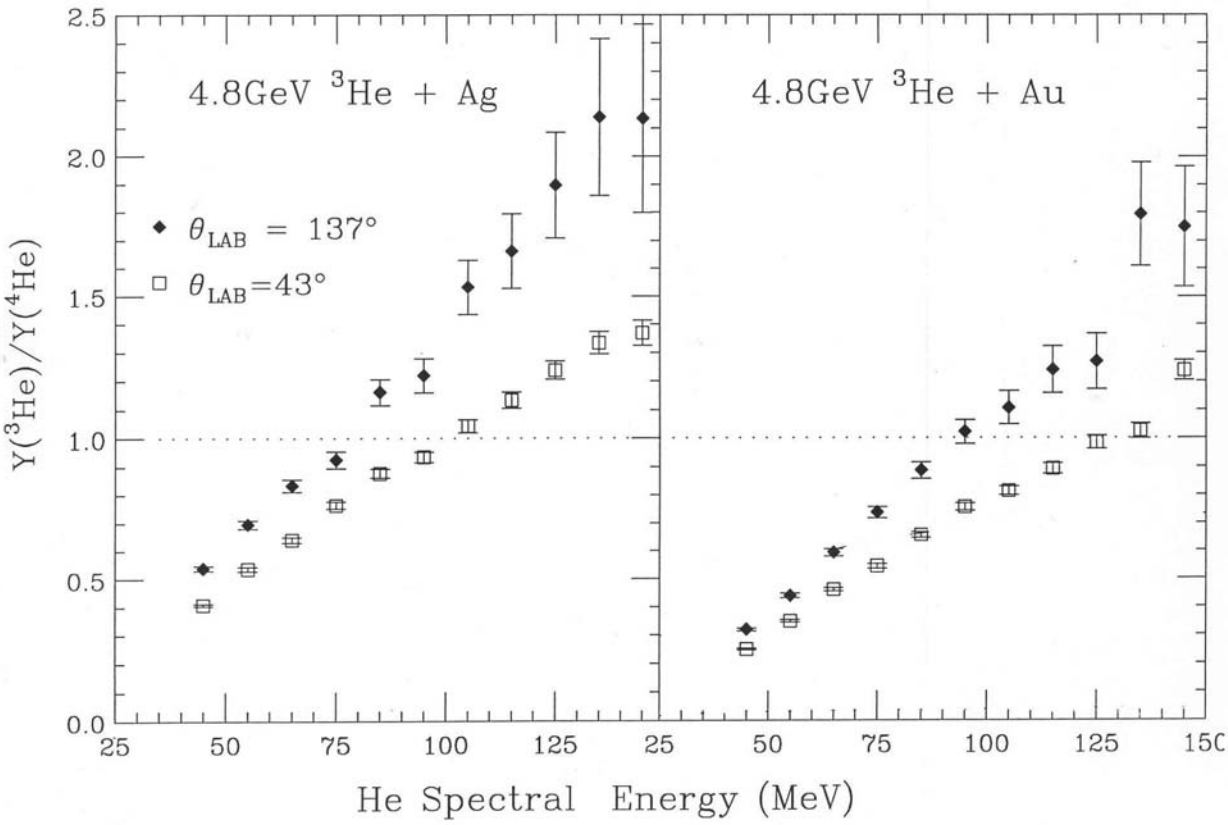
4.8GeV ^{3}He + Ag
4.8GeV ^{3}He + Au
θ_{LAB} = 137°
θ_{LAB}=43°
Y(^{3}He)/Y(^{4}He)
He Spectral Energy (MeV)
0.0
0.5
1.0
1.5
2.0
2.5
25
50
75
100
125
150

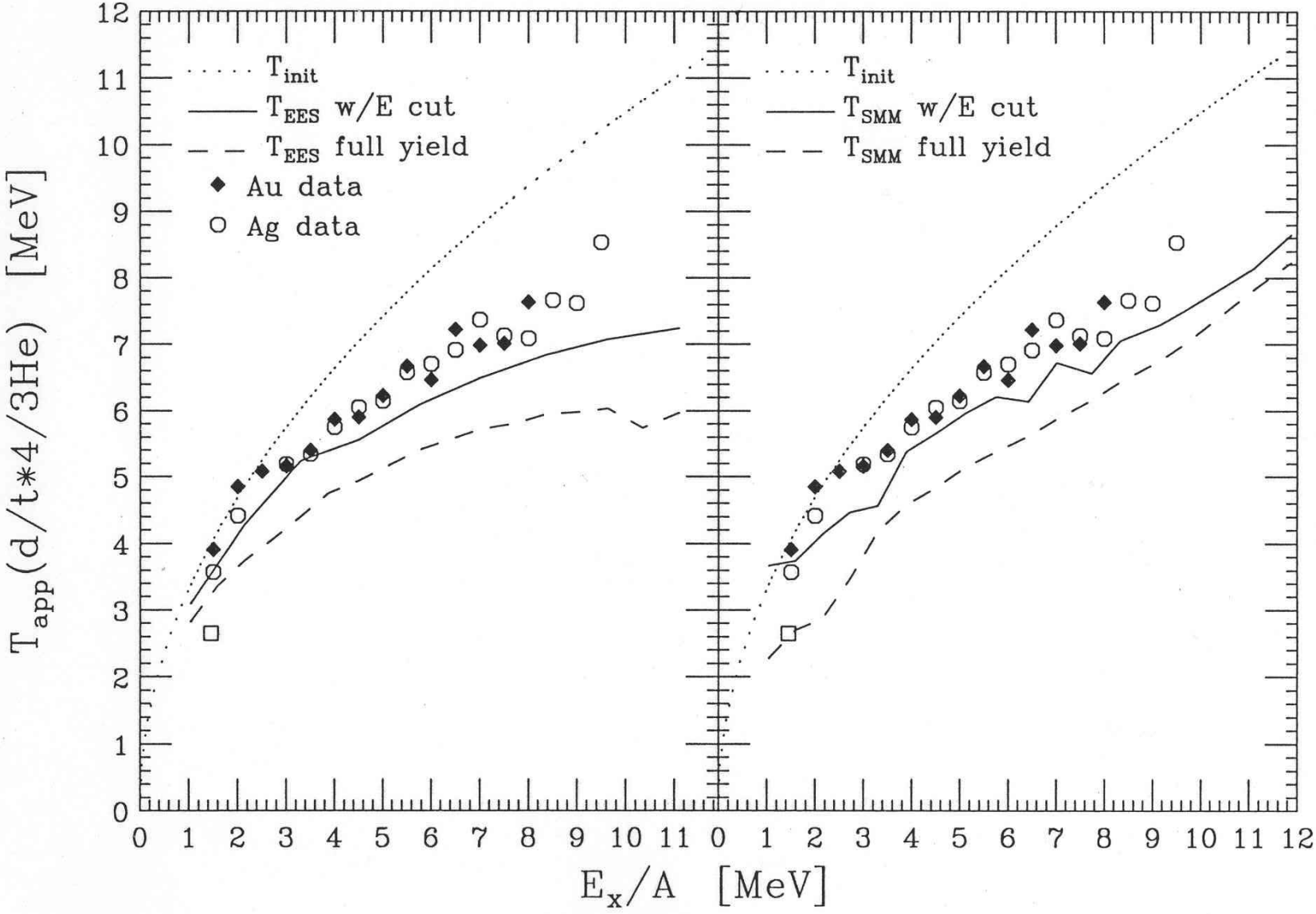
4.8GeV ^{3}He+Ag, Au vs EES & SMM on Au
T_{init}
T_{EES} w/E cut
T_{EES} full yield
Au data
Ag data
T_{init}
T_{SMM} w/E cut
T_{SMM} full yield
T_{app}(d/t*4/3He) [MeV]
E_x/A [MeV]